NEUTRON STARS

Multimessenger constraints on the neutron-star equation of state and the Hubble constant

Tim Dietrich[1,2]*, Michael W. Coughlin[3], Peter T. H. Pang[2,4], Mattia Bulla[5], Jack Heinzel[3,6,7], Lina Issa[5,8], Ingo Tews[9], Sarah Antier[10]

Observations of neutron-star mergers with distinct messengers, including gravitational waves and electromagnetic signals, can be used to study the behavior of matter denser than an atomic nucleus and to measure the expansion rate of the Universe as quantified by the Hubble constant. We performed a joint analysis of the gravitational-wave event GW170817 with its electromagnetic counterparts AT2017gfo and GRB170817A, and the gravitational-wave event GW190425, both originating from neutron-star mergers. We combined these with previous measurements of pulsars using x-ray and radio observations, and nuclear-theory computations using chiral effective field theory, to constrain the neutron-star equation of state. We found that the radius of a 1.4–solar mass neutron star is $11.75^{+0.86}_{-0.81}$ km at 90% confidence and the Hubble constant is $66.2^{+4.4}_{-4.2}$ at 1σ uncertainty.

Multimessenger observations of binary neutron star (BNS) mergers, which use different probes to observe the same astrophysical process, elucidate the properties of matter under extreme conditions and can be used to determine the Hubble constant, which quantifies the expansion rate of the Universe. An example was the joint detection of gravitational waves (GWs) and their electromagnetic (EM) counterparts from the same astrophysical source: the GW event GW170817 (*1*), the gamma-ray burst (GRB) GRB170817A, its GRB afterglow arising from synchrotron radiation (*2*), and the kilonova AT2017gfo—an EM signal in the optical, infrared, and ultraviolet bands originating from the radioactive decay of atomic nuclei created during a merger (*3*). Using only GWs and the redshift of the host galaxy, this event led to an independent measurement of the Hubble constant (*4*). It also placed constraints on the equation of state (EOS) of matter at densities higher than in the center of an atomic nucleus [for example, (*5*)]. GWs have also been detected from another BNS merger, GW190425 (*6*), but no EM counterpart was observed (*7*). Joint observations of the mass and radius of the rapidly rotating neutron star (pulsar) PSR J0030+0451 by the Neutron Star Interior Composition Explorer (NICER) [for example, (*8*)] have provided independent constraints on neutron star properties (*9*). These build on mass measurements of the pulsars PSR J0740+6620 (*10*), PSR J0348+4042 (*11*), and PSR J1614-2230 (*12*) using radio observations.

We combined the results from GW170817, GW190425, AT2017gfo, GRB170817A, PSR J0030+0451, PSR J0740+6620, PSR J0348+4042, and PSR J1614-2230 with nuclear-theory calculations of the EOS, the latter by using chiral effective field theory (EFT) predictions at low densities (*13*). Previous studies have connected GW analyses to nuclear-physics predictions (*14*, *15*), performed Bayesian analyses of EM and GW signals (*16*, *17*), or combined GW and NICER results (*18*, *19*). We combined all of these approaches, with the goal of providing improved constraints on the supranuclear EOS and measuring the Hubble constant.

We used a multistep procedure (Fig. 1) to incorporate constraints from nuclear theory and from astrophysical observations. Our analysis began by constructing a set of 5000 EOSs (*13*) that provide possible descriptions of the structure of neutron stars (Fig. 1A). At low densities, these EOSs are constrained by microscopic calculations that use chiral EFT interactions and computational many-body methods. Chiral EFT is a systematic theory for nuclear forces that describes the interactions in terms of nucleon and pion degrees of freedom and is consistent with the symmetries of quantum chromodynamics (*20*). The resulting forces are arranged in an order-by-order expansion, which is then truncated at a certain level. This systematic scheme allows for the estimation of theoretical uncertainties from missing higher-order contributions to the nuclear interactions. The resulting nuclear Hamiltonians are inserted into the Schrödinger equation, which has been solved by using quantum Monte Carlo methods (*21*). Chiral EFT might be valid up to $2n_{\rm sat}$ (*22*), where $n_{\rm sat} = 0.16$ fm^{-3} is the nuclear saturation density. Beyond that, chiral EFT interactions and their uncertainty estimates are not reliable. We adopted a more conservative limit and constrained our EOSs with chiral EFT calculations up to densities of $1.5n_{\rm sat}$. At densities above that limit, we used a model-agnostic parametric expansion scheme that represents the EOS in the speed of sound plane (*22*) and ensures consistency with causality.

We then restricted the set of EOSs by including astrophysical constraints. First, we began by enforcing a maximum neutron star mass $M_{\rm max}$ with an upper bound of $M_{\rm max} \leq 2.16^{+0.17}_{-0.15}$ solar masses ($M_\odot$) at 2σ uncertainty (*13*, *23*). This upper bound was derived by assuming that the final merger remnant of GW170817 was a black hole (*23*). We derived a lower bound for the maximum mass by combining radio observations of PSR J0740+6620 (*10*), PSR J0348+4042 (*11*), and PSR J1614-2230 (*12*). The resulting distribution for the maximum mass and the updated EOS set are shown in Fig. 1B. For comparisons with other works, we calculated the radius of a typical 1.4 $M_\odot$ neutron star at 90% confidence. The corresponding radii at each stage of our analysis are shown in Fig. 1H.

Second, we included the NICER results (*13*) using the joint posterior probability density function for mass and radius from the best fitting model of (*8*), shown in Fig. 1C. We assigned a probability to each EOS on the basis of the maximum neutron star mass and NICER constraints.

Third, by sampling over the obtained EOS set by using their precomputed probabilities, we analyzed GW170817 (*13*). Neutron star properties are inferred from GW signals through tidal effects that are larger for neutron stars with smaller masses and larger radii. We used the PARALLEL BILBY software (*24*) and the GW waveform model IMRPhenomPv2_NRTidalv2 (*25*) for cross-correlation with the observed GW data (*1*), inferring the binary properties from the measured signal. This model is an updated version of the waveform approximant IMRPhenomPv2_NRTidal, which has been used in previous analyses of GW170817 (*26*) and GW190425 (*6*).

Fourth, we added constraints from AT2017gfo using a published light curve model (*13*, *27*). We used a Gaussian-process-regression framework to compute generic light curves for various ejecta-mass properties. To connect the individual ejecta parameters to the properties of the system, we assumed that the total ejecta mass $M_{\rm ej}$ is a sum of multiple components: dynamical ejecta $M_{\rm ej}^{\rm dyn}$, the material released during the merger process through shocks and torque, and disk-wind ejecta $\zeta M_{\rm disk}$, so that $M_{\rm ej} =$

[1]Institut für Physik und Astronomie, Universität Potsdam, 14476 Potsdam, Germany. [2]Nikhef, 1098 XG Amsterdam, Netherlands. [3]School of Physics and Astronomy, University of Minnesota, Minneapolis, MN 55455, USA. [4]Department of Physics, Utrecht University, 3584 CC Utrecht, Netherlands. [5]Nordic Institute for Theoretical Physics (Nordita), 106 91 Stockholm, Sweden. [6]Department of Physics and Astronomy, Carleton College, Northfield, MN 55057, USA. [7]Artemis, Université Côte d'Azur, Centre National de la Recherche Scientifique, F-06304 Nice, France. [8]École normale supérieure, Université Paris-Saclay, 91190 Gif-sur-Yvette, France. [9]Theoretical Division, Los Alamos National Laboratory, Los Alamos, NM 87545, USA. [10]Astroparticule et Cosmologie, Université de Paris, Centre National de la Recherche Scientifique, F-75013 Paris, France.
*Corresponding author. Email: tim.dietrich@uni-potsdam.de

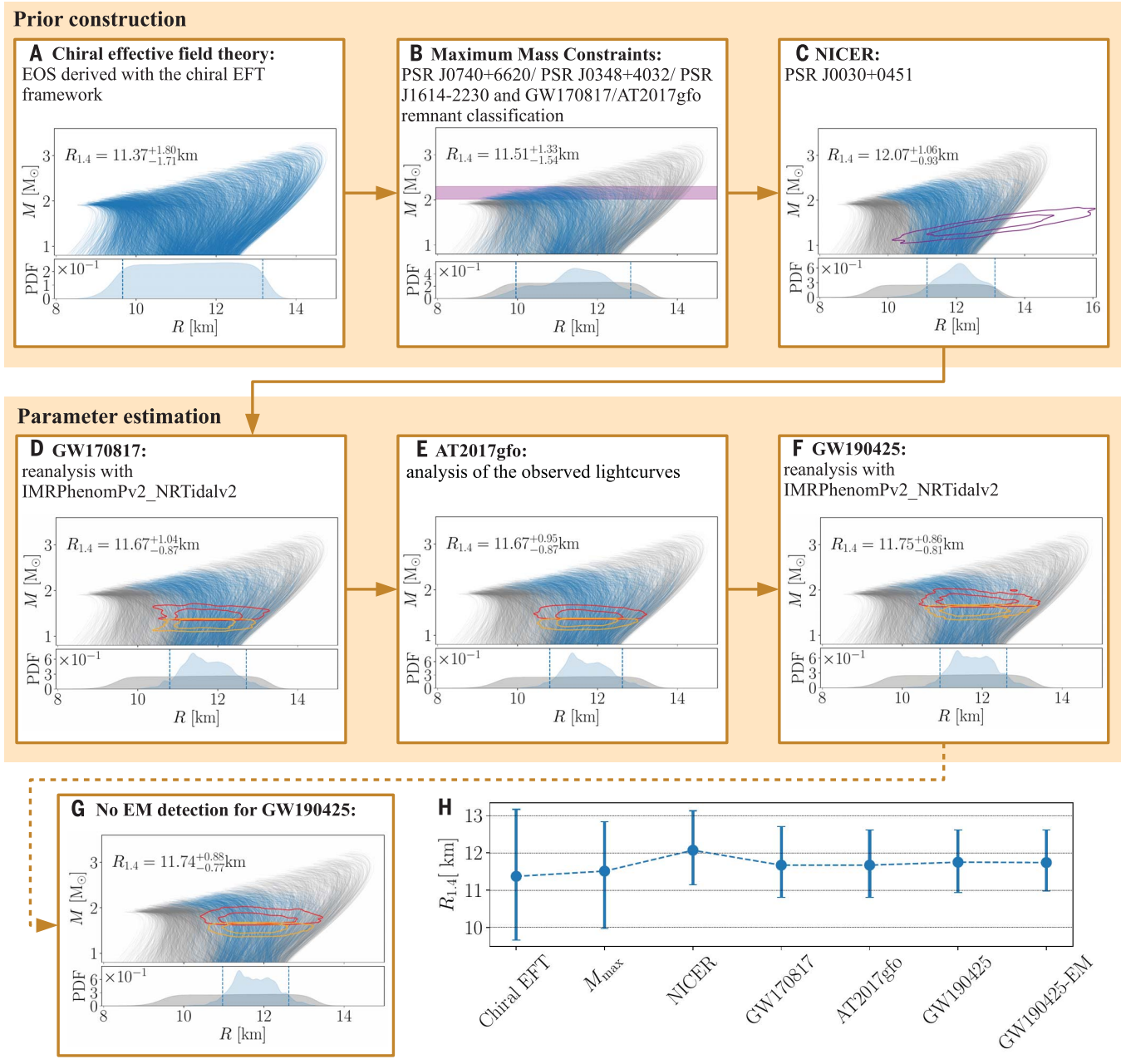

Fig. 1. Multistep procedure to constrain the neutron-star EOS. In (A) to (H), allowed EOSs are shown as blue lines, and disallowed EOSs are shown as gray lines. Lower plots indicate the probability distribution function (PDF) for the radius of a 1.4 $M_\odot$ neutron star, with the 90% confidence range indicated by dashed lines. (**A**) The set of EOSs from chiral EFT. (**B**) The EOS set restricted by incorporating information from mass measurements of PSR J0740+6620, PSR J0348+4032, PSR J1614-2230, and the maximum-mass constraints obtained from GW170817/AT2017gfo. The 90% confidence interval of the maximum mass posterior probability distribution is indicated by a purple band. (**C**) The EOS set further restricted by the NICER mass-radius measurement of PSR J0030+0451 (purple contours at 68 and 95% confidence). (**D**) Further restriction of the EOS set by using Bayesian inference from our reanalysis of the GW170817 waveform. Contours at 68 and 95% confidence show the mass-radius measurements of the primary (red) and secondary (orange) neutron stars. (**E**) Analysis of AT2017gfo by using the chirp mass, mass ratio, and the EOSs as Bayesian priors. (**F**) Further restrictions by analyzing GW190425. This is our fiducial result. (**G**) Additional analysis assuming that GW190425 did not produce a detectable EM signal. (**H**) The radius constraint at each step of this analysis, with 90% confidence ranges.

$M_{ej}^{dyn} + \zeta M_{disk} + \alpha$. The free parameters α, corresponding to a potentially unmodeled ejecta component, and ζ, determining how much mass of the disk is ejected, are unknowns. Our treatment of the dynamical ejecta follows previous work (*16*). Existing disk-wind ejecta models are known to be inappropriate for systems with high mass ratios. To overcome this issue, we included an explicit mass-ratio dependence in the disk-mass prediction (*13*). The GW results for the chirp mass $\mathcal{M}_c = (m_1 m_2)^{3/5}(m_1 + m_2)^{-1/5}$—with m_1 and m_2 being the masses of the heavier and lighter neutron stars, respectively—the mass ratio $q = m_1 m_2^{-1}$, and the EOS were used as priors for our analysis of AT2017gfo. This further constrains the EOS models (Fig. 1D). Including all steps so far, we obtained the radius of a

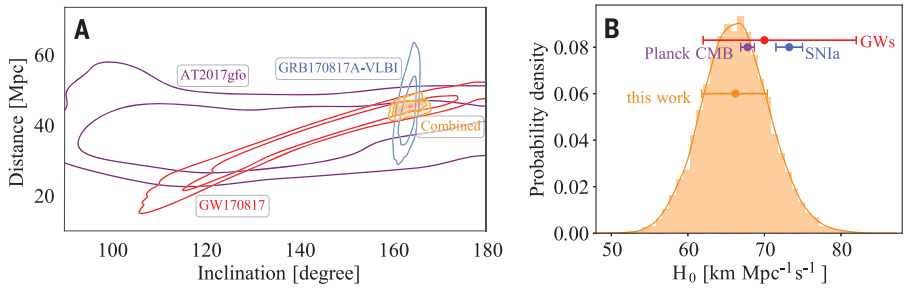

Fig. 2. Distance-inclination constraints and Hubble constant measurement. (**A**) Estimated distance and inclination of GW170817 from the GW waveform (red), AT2017gfo analysis (purple), and the radio interferometry constraint (*29*) derived from GRB170817A (blue). The combined distance-inclination measurement is shown in orange. Contours are shown at 68 and 95% confidence. (**B**) Hubble constant estimate from our combined inclination measurement (orange histogram). Symbols mark the most probable values and 1σ uncertainties from this work (orange), the Planck measurement of the cosmic microwave background (Planck CMB; purple) (*31*), the Hubble measurement via type-Ia supernovae (SNIa; blue) (*30*), and the Hubble estimate from GW170817 alone (GWs; red) (*4*).

1.4 $M_\odot$ neutron star of $R_{1.4M_\odot} = 11.67^{+0.95}_{-0.87}$ km at 90% confidence.

These results can be further constrained by combining them with another observed BNS merger, GW190425 (*6*). Because of the high total mass of GW190425 of $3.4^{+0.3}_{-0.1} M_\odot$ at 90% confidence, which suppresses tidal effects, we found (*13*) that the inclusion of GW190425 does not improve the precision but does slightly shift the median value within the uncertainty. Our final estimate on the radius of a 1.4 $M_\odot$ neutron star is $R_{1.4M_\odot} = 11.75^{+0.86}_{-0.81}$ km, with 90% confidence. We also explored an alternative ordering of individual analysis steps (fig. S11) and systematic uncertainties because of the use of different GW models (fig. S12), finding a consistent radius constraint (supplementary text).

Several independent EM searches for counterparts to GW190425 observed large fractions of the possible sky area (supplementary text) (*7*), suggesting that most of the appropriate region was searched, but no EM signal was detected. To include this nondetection, we used the same kilonova analysis as for GW170817, combining it with upper limits reported by the optical EM counterpart searches. Using the distance information from the GW data, 159^{+69}_{-71} Mpc at 90% confidence level (*6*), we obtained limits on the absolute magnitude of a potential counterpart. Using our light curve models, we ruled out parts of the parameter space for which the predicted absolute magnitude would be above the obtained limit. Following this procedure, we arrived at a radius estimate of $R_{1.4M_\odot} = 11.74^{+0.88}_{-0.77}$ (90% confidence) under the assumption that if GW190425 produced a detectable signal, it would have been found. To be conservative, we omitted this step from the subsequent analysis.

Our study includes information from GW170817; AT2017gfo; GRB170817A; GW190425; the NICER observation of PSR J0030+0451; and the radio observations of PSR J0740+6620, PSR J0348+4032, and PSR J1614-2230. Our approach allows for strong phase transitions in the EOS, the combination of multiple events, and the incorporation of EM nondetections. We compare our final result of $R_{1.4M_\odot} = 11.75^{+0.86}_{-0.81}$ km with a selection of previous studies in Table 1. The inclusion of additional astrophysical observations does not necessarily lead to tighter constraints (Fig. 1H) because (i) the full combined posterior probability distributions are incorporated in the analysis and (ii) the number of events detected with multiple messengers remains very small.

In addition to EOS constraints, we performed a measurement of the Hubble constant (*13*). For this purpose, we assumed that measurable properties related to the kilonova, such as time scale and color evolution of the ejecta, are connected to its intrinsic luminosity. Theoretical kilonova predictions can be used to standardize kilonovae light curves and thereby measure their distances (*28*). Combining the distance measurement with the redshift z of the host galaxy NGC 4993, $z = 0.009783 \pm 0.000023$, constrains the Hubble constant (*4*). We combined the distance and inclination measurements of the GW and kilonova analyses with the measurement using radio observations of the GRB afterglow (Fig. 2) (*13*, *29*). The comparison of a kilonova observation with a light curve model permits a large parameter range, owing to the complexity of the model. Adopting two other kilonova models (supplementary text) indicates that our kilonova constraints are conservative, but it is not possible to test the robustness of different kilonova models with only one well-sampled kilonova observation (AT2017gfo). Combining all of these measurements leads to an improved distance constraint

Table 1. Comparison with selected radius constraints from multimessenger observations. For each reference, we indicate whether chiral EFT input, constraints from heavy-pulsar mass measurements (Heavy PSRs), maximum-mass constraints obtained from GW170817/AT2017gfo (M_{max}), GW constraints from GW170817 or GW190425, constraints from kilonova light curves (AT2017gfo), constraints from the GRB afterglow (GRB170817A), and constraints from NICER were used. We indicate with a checkmark where either the full posterior probability distribution or a Bayesian inference was used, an open circle where some information was included without performing a Bayesian analysis or including the full posterior probability distribution, and an "X" where the information was not included in the study. Stated radius uncertainties represent 90% confidence intervals, and for (*17*), we also include systematic uncertainties as stated by those authors.

Reference	Chiral EFT	Heavy PSRs	M_{max} (remnant)	GW1700817	AT2017gfo	GRB170817A	NICER	GW190425	$R_{1.4\,M_\odot}$ [km]
This work	Yes	√	√	√	√	√	√	√	$11.75^{+0.86}_{-0.81}$
(*19*)	Yes	√	✗	√	✗	✗	√	✗	[11.63, 13.26]
(*15*)	Yes	○	○	√	✗	✗	✗	✗	$11.0^{+0.9}_{-0.6}$
(*16*)	No	√	○	√	√	○	✗	✗	[11.3, 13.5]
(*17*)	No	✗	✗	√	○	✗	✗	✗	$(12.2^{+1.0}_{-0.8} \pm 0.2)$
(*5*)	No	○	✗	√	✗	✗	✗	✗	$11.9^{+1.4}_{-1.4}$
(*14*)	Yes	○	✗	○	✗	✗	✗	✗	[9.9, 13.6]

and an estimate of the Hubble constant of $H_0 = 66.2^{+4.4}_{-4.2}$ at 1σ uncertainty (Fig. 2B). We found that the radio inclination measurement reduces the existing uncertainty on the Hubble constant by more than the kilonova measurement, at least for this single event. The uncertainty does not allow us to resolve the tension between measurements through type-Ia supernovae (*30*) and the Planck measurement of the cosmic microwave background (*31*), but our results indicate a preference for the latter (Fig. 2B).

REFERENCES AND NOTES

1. B. P. Abbott *et al*., LIGO Scientific Collaboration and Virgo Collaboration, *Phys. Rev. Lett.* **119**, 161101 (2017).
2. B. P. Abbott *et al*., *Astrophys. J.* **848**, L13 (2017).
3. B. Abbott *et al*., *Astrophys. J.* **848**, L12 (2017).
4. A. Abbott, *Nature* **551**, 425–426 (2017).
5. B. P. Abbott *et al*., LIGO Scientific Collaboration and the Virgo Collaboration, *Phys. Rev. Lett.* **121**, 161101 (2018).
6. B. Abbott *et al*., *Astrophys. J.* **892**, L3 (2020).
7. M. W. Coughlin *et al*., *Mon. Not. R. Astron. Soc.* **492**, 863–876 (2020).
8. M. C. Miller *et al*., *Astrophys. J.* **887**, L24 (2019).
9. G. Raaijmakers *et al*., *Astrophys. J.* **887**, L22 (2019).
10. H. T. Cromartie *et al*., *New Astron.* **4**, 72–76 (2019).
11. J. Antoniadis *et al*., *Science* **340**, 448, 1233232 (2013).
12. Z. Arzoumanian *et al*., *Astrophys. J. Suppl. Ser.* **235**, 37 (2018).
13. Materials and methods are available as supplementary materials.
14. E. Annala, T. Gorda, A. Kurkela, A. Vuorinen, *Phys. Rev. Lett.* **120**, 172703 (2018).
15. C. D. Capano *et al*., *New Astron.* **4**, 625–632 (2020).
16. M. W. Coughlin, T. Dietrich, B. Margalit, B. D. Metzger, *Mon. Not. R. Astron. Soc. Lett.* **489**, L91–L96 (2019).
17. D. Radice, L. Dai, *Eur. Phys. J. A* **55**, 50 (2019).
18. J.-L. Jiang, S.-P. Tang, Y.-Z. Wang, Y.-Z. Fan, D.-M. Wei, *Astrophys. J.* **892**, 1 (2020).
19. G. Raaijmakers *et al*., *Astrophys. J.* **893**, L21 (2020).
20. E. Epelbaum, H.-W. Hammer, U.-G. Meissner, *Rev. Mod. Phys.* **81**, 1773–1825 (2009).
21. J. Carlson *et al*., *Rev. Mod. Phys.* **87**, 1067–1118 (2015).
22. I. Tews, J. Carlson, S. Gandolfi, S. Reddy, *Astrophys. J.* **860**, 149 (2018).
23. L. Rezzolla, E. R. Most, L. R. Weih, *Astrophys. J.* **852**, L25 (2018).
24. R. J. E. Smith, G. Ashton, A. Vajpeyi, C. Talbot, *Mon. Not. R. Astron. Soc.* **498**, 4492–4502 (2020).
25. T. Dietrich *et al*., *Phys. Rev. D* **100**, 044003 (2019).
26. B. P. Abbott *et al*., *Phys. Rev. X* **9**, 011001 (2019).
27. M. Bulla, *Mon. Not. R. Astron. Soc.* **489**, 5037–5045 (2019).
28. M. W. Coughlin *et al*., *Phys. Rev. Res.* **2**, 022006 (2020).
29. K. Hotokezaka *et al*., *New Astron.* **3**, 940–944 (2019).
30. A. G. Riess *et al*., *Astrophys. J.* **826**, 56 (2016).
31. P. A. R. Ade *et al*., *Astron. Astrophys.* **594**, A13 (2016).
32. T. Dietrich *et al*., Multi-messenger constraints on the neutron-star equation of state and the Hubble constant – Data and Codes. Zenodo (2020); doi:10.5281/zenodo.4114141.

ACKNOWLEDGMENTS

We thank K. Hotokezaka for providing the posterior probability distribution samples from (*29*). We are also grateful to Z. Doctor, R. Essick, and the anonymous referees for helpful comments on the manuscript. **Funding:** T.D. acknowledges support by the European Union's Horizon 2020 research and innovation program under grant agreement 749145, BNSmergers. M.W.C. acknowledges support from the National Science Foundation with grant PHY-2010970. P.T.H.P. is supported by the research program of the Netherlands Organization for Scientific Research (NWO). J.H. acknowledges support from the National Science Foundation with REU grant NSF1757388. I.T. is supported by the U.S. Department of Energy, Office of Science, Office of Nuclear Physics, under contract DE-AC52-06NA25396; by the Laboratory Directed Research and Development program of Los Alamos National Laboratory under project 20190617PRD1; and by the U.S. Department of Energy, Office of Science, Office of Advanced Scientific Computing Research, Scientific Discovery through Advanced Computing (SciDAC) program. S.A. is supported by the CNES Postdoctoral Fellowship at Laboratoire Astroparticle et Cosmologie. The authors gratefully acknowledge the Gauss Centre for Supercomputing e.V. for funding this project by providing computing time on the GCS Supercomputer SuperMUC at Leibniz Supercomputing Centre. Computations were performed on the Minerva HPC cluster of the Max Planck Institute for Gravitational Physics, on SuperMUC-NG (LRZ) under project pn56zo, and on HAWK (HLRS) under project 44189. Computational resources were also provided by the Los Alamos National Laboratory Institutional Computing Program, which is supported by the U.S. Department of Energy National Nuclear Security Administration under contract 89233218CNA000001, and by the National Energy Research Scientific Computing Center (NERSC), which is supported by the U.S. Department of Energy, Office of Science, under contract DE-AC02-05CH11231. **Author contributions:** Conceptualization: T.D., M.W.C., M.B., and I.T. Methodology: T.D., M.W.C., P.T.H.P., M.B., J.H., L.I., I.T., and S.A. Software: T.D., M.W.C., P.T.H.P., M.B., J.H., L.I., and I.T. Validation: T.D., M.W.C., P.T.H.P., M.B., and I.T. Formal analysis: T.D., M.W.C., P.T.H.P., and I.T. Resources: T.D., M.W.C., and I.T. Data curation: T.D., M.W.C., P.T.H.P., J.H., and I.T. Writing, original draft: T.D., M.W.C., P.T.H.P., M.B., and I.T. Writing, review and editing: T.D., M.W.C., P.T.H.P., J.H., L.I., I.T., and S.A. Visualization: T.D., M.W.C., and P.T.H.P. Supervision: T.D., M.W.C., and I.T. Project administration: T.D., M.W.C., and I.T. Funding acquisition: T.D., M.W.C., and I.T. **Competing interests:** We declare no competing interests. **Data and Materials availability:** Full posterior data samples of our analysis and code necessary to reproduce the study are available at https://github.com/diettim/NMMA and archived at (*32*). All GW models we used are implemented in the publicly available software LALSUITE at https://git.ligo.org/lscsoft. The BILBY and PARALLEL BILBY codes are available at https://git.ligo.org/lscsoft/bilby and https://git.ligo.org/lscsoft/parallel_bilby, respectively. The GWEMLIGHTCURVE software is available at https://gwemlightcurves.github.io. The exact versions of BILBY, PARALLEL BILBY, LALSUITE, and GWEMLIGHTCURVE that we used are also archived at (*32*). The GW data that were obtained from the Gravitational Wave Open Science Center (GWOSC) are available at https://www.gw-openscience.org, and the NICER data were taken from doi:10.5281/zenodo.3473466.

SUPPLEMENTARY MATERIALS

science.sciencemag.org/content/370/6523/1450/suppl/DC1
Materials and Methods
Supplementary Text
Figs. S1 to S13
Tables S1 to S3
References (*33*–*111*)

24 February 2020; accepted 27 October 2020
10.1126/science.abb4317

Multimessenger constraints on the neutron-star equation of state and the Hubble constant

Tim Dietrich, Michael W. Coughlin, Peter T. H. Pang, Mattia Bulla, Jack Heinzel, Lina Issa, Ingo Tews and Sarah Antier

Science **370** (6523), 1450-1453.
DOI: 10.1126/science.abb4317

A combined multimessenger analysis

Neutron stars are stellar remnants with densities greater than that of an atomic nucleus. The properties of matter under such extreme conditions are poorly understood and inaccessible to terrestrial laboratories. Dietrich *et al.* developed a framework to combine multiple constraints on the masses and radii of neutron stars, including data from gravitational waves, electromagnetic observations, and theoretical nuclear physics calculations. They used this analysis to constrain the neutron-star equation of state and also improved the precision on the gravitational wave (standard siren) measurement of the Hubble constant—the expansion rate of the Universe.

Science, this issue p. 1450